Near-Field Bessel-Gauss Antenna for Non-Metal Internal Defects Detection

This article has been accepted for publication in a future issue of this journal, but has not been fully edited. Content may change prior to final publication. Citation information: DOI 10.1109/LAWP.2021.3115166, IEEE Antennas and Wireless Propagation Letters

Near-Field Bessel-Gauss Antenna for Non-Metal Internal Defects Detection

Xiaoqing Yang, Weize Li, Ping Lu, *Member, IEEE,* Qian Liu, Ying Zou, Yi Xie, Chaoyun Song, *Member, IEEE* and Yunfeng Qiu

***Abstract*—A Radial Line Slot Array (RLSA) is proposed for Bessel-Gauss beam generation with a narrow main beamwidth and low sidelobe characteristics for non-metallic internal defects detection. Owing to the radial attenuation factor of Gaussian function, the sidelobe level of Bessel-Gauss beam can be suppressed. By accurately adjusting the slot position and size of the RLSA, the optimum aperture field distribution can be synthesized to generate the near-field Bessel-Gauss beam based on the projection method. The simulated/measured results have shown that the maximum non-diffraction distance of 70mm/70mm and the null-null beam width (NNBW) of the Bessel-Gauss main beam of 30mm/30mm are achieved at the operating frequency of 12.5 GHz/12.5 GHz, whilst low sidelobe levels (<-18.14dB/-18.07dB) are generated. Compared to other antennas for microwave nondestructive testing (NDT), the proposed RLSA has merits of low sidelobes, large E-field depth and narrow main beam, therefore it can improve the detection performance in terms of sensitivity and depth, which can be widely used for non-metal internal defects detection applications.**

***Index Terms*—Bessel-Gauss Beam, Low sidelobes, Microwave nondestructive testing, Non-metal detection, Projection method, Radial Line Slot Array (RLSA).**

I. Introduction

NON-METALLIC composite materials as a substitution of metallic materials are widely used in aerospace, automotive manufacturing and civil engineering, since these materials have advantages in such as lightness, high strength, easy manufacturing and low cost [1]. For the limitations of the unpredictable environment and processing technology, debonding, wrinkling and delamination can be formed during the composite materials molding as well as the use of the composite materials, which leads to poor performance of such non-metal materials.

This work was supported in part by the Guizhou Aerospace Institute of Measuring and Testing Technology (HG2020192), (JZX7J20191201ZL0002); Defense Technology Innovation Rapid Response Team (19-163-00-KX-002-016-02); National Natural Science Foundation of China (No.51907130); Sichuan Science and Technology Program: Provincial Overseas Cooperation Grant (No.2020YFH0091) and Chengdu Science and Technology Program under Grant (No. 2020-GH02-00036-HZ). (Corresponding author: Ping Lu. e-mail: pinglu90@scu.edu.cn)

X. Yang, W. Li, P. Lu, Q. Liu, Y. Zou are with the College of Electronics and Information Engineering, Sichuan University, Chengdu 610065, China.

Y. Xie is with the College of Electronics and Information Engineering, Sichuan University, Chengdu 610065, China, and also with the College of Electronic Engineering, Chengdu University of Information Technology, Chengdu 610225, China.

C. Song is with the School of Engineering and Physical Sciences, Heriot-Watt University, Edinburgh EH14 4AS, Scotland, UK.

Y. Qiu is with the Guizhou Aerospace Institute of Measuring and Testing Technology, Guizhou 550009, China.

To detect the internal defects of non-metal materials, the near-field microwave nondestructive testing (NDT) technology is an effective and reliable method, compared to other methods for detecting internal defects in non-metal such as ultrasonic and transient thermography [2]. By using microwaves, the non-metal materials could be easily penetrated, and the device under test (DUT) without any physical contacts can be detected effectively and quickly.

So far, many works regarding the near-field microwave NDT methods have been reported, including the dual-polarized waveguide [3], open-ended rectangular waveguide [4], horn antenna [5] etc. These waveguide probe methods are able to characterize the existence of internal defects in non-metal composites. But low sensitivity and shallow detection depth are observed. Typically, the size of the detectable defect is inversely proportional to the wavelength, therefore, the costly millimeter-wave detector would be required [6].

Recently, non-diffractive beam, i.e. the main beam does not diffract within the propagation distance, has been used in near-field microwave NDT. In [7], a Radial Line Slot Array (RLSA) with the non-diffractive Bessel beam generation was used to detect buried objects, which proved the prominent advantages of the non-diffractive beam in such detection applications. Due to the intrinsic low cost and planarity, many RLSA structures have been designed to generate Bessel beams [8]-[11]. However, the high sidelobes of these Bessel beams was detrimental for defect detection. In particular, the defects in the non-target detection area could be sensed by high sidelobes, thereby causing the inaccurate detection of damage locations.

To suppress the sidelobes, Gaussian function with radial attenuation factor is introduced to modulate the Bessel function to the Bessel-Gauss beam [13], which has the characteristics of non-diffraction, narrow beam width and low sidelobe level. In recent years, some Bessel-Gauss generators have been proposed [13]-[16]. In [13]-[15], the scalar theory of paraxial approximation is used for Bessel-Gauss beam generation. However, the paraxial approximation can hardly be applied to the microwave range, where the vectorial nature of the electromagnetic fields cannot be neglected [16]. Even though some scalar design approaches have been adopted in the microwave frequency range, they are only valid when the aperture size is much larger than the wavelength of interest, and for small transverse wavenumbers (k_ρ<0.3k_0). Besides, by using the vector method, the leaky wave structure was designed to generate a modulated Bessel-Gauss beam. However, the synthesis procedure was complicated, and the proposed leaky wave structure had a large thickness [16]-[17].

This article has been accepted for publication in a future issue of this journal, but has not been fully edited. Content may change prior to final publication. Citation information: DOI 10.1109/LAWP.2021.3115166, IEEE Antennas and Wireless Propagation Letters

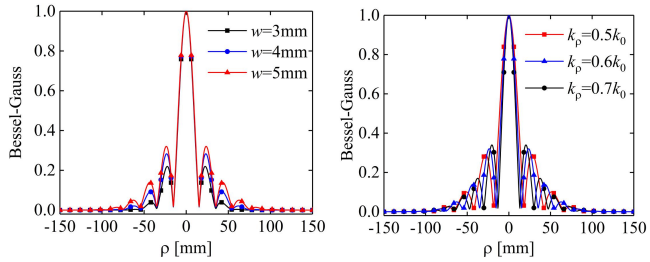

(a) (b)

Fig. 1. Bessel-Gauss profiles with different w and k_ρ. (a) With different w (b) With different k_ρ.

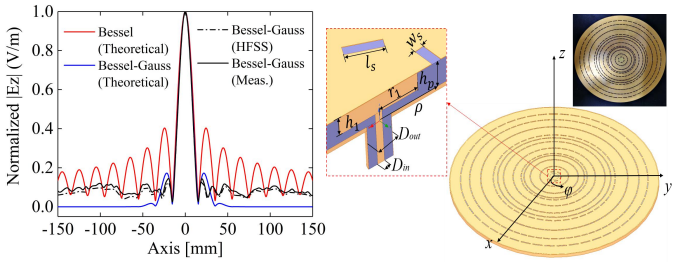

(a) (b)

Fig. 2. Bessel-Gauss profiles and RLSA structure. (a) Bessel beam and Bessel-Gauss beam profiles at z=50mm. (b) Geometrical structure of RLSA antenna. The radius of each ring is ρ_i. The slots on each ring have the same length l_s. The width of the slots is constant, i.e. w_s=1.5mm. The diameter of inner conductor D_{in} is 1.2mm and outer conductor D_{out} is 4.1mm. The radius (r_1) of the disc is 6.95mm and the thickness (h_1) of the disc is 2mm.

In this letter, a RLSA Bessel-Gauss antenna is designed by using a projection method [18], which is an effective synthesis procedure being alternative to the leaky wave method. Through the MATLAB-HFSS co-simulation, the layout of the slot array i.e. slot position and slot size, is optimally deployed for the target Bessel-Gauss distribution. Compared to the horn antennas and open-ended waveguides for near-field microwave NDT, the Bessel-Gauss non-diffractive antenna with low sidelobes can achieve large detection depth with excellent sensitivity.

II. Bessel-Gauss Beam

This section briefly summarizes the theoretical analysis of Bessel-Gauss beams. Due to the symmetry of the radial waveguide, the field distribution is invariant along φ and is only a function of ρ. In a cylindrical coordinate system, the Bessel-Gauss function can be expressed as

$$E_z(\rho, z) = J_0(k_\rho \rho) e^{-jk_z z} e^{-\rho^2/w^2} \quad (1)$$

where $J_0(k_\rho\rho)$ is the zero-order Bessel distribution and $e^{-(\rho^2/w^2)}$ is attenuation factor of the Gaussian function. k_ρ is the radial wavenumber, $k_z = \sqrt{k_0^2 - k_\rho^2}$. $w = w_0\sqrt{1 + (z/z_R)^2}$ is the beam waist radius of the Gaussian function at the transmission distance z. The Rayleigh distance is $z_R = k_0 w_0^2/2$ and w_0 is the beam waist radius of the Gaussian function at z=0.

Fig. 1 shows the Bessel-Gauss profiles at different w and k_ρ.

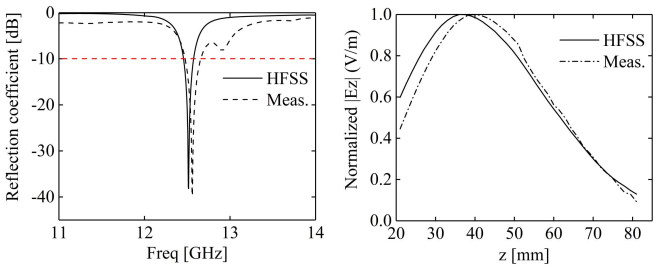

(a) (b)

Fig. 3. Simulated and measured of the proposed RLSA antenna. (a) Reflection coefficient. (b) Normalized $|E_z|$ profiles along the Oz-axis.

TABLE I
POSITION AND DIMENSIONS OF SLOTS IN THE RLSA

Ring number	1	2	3	4	5	6
ρ_i[mm]	8.95	19.7	33.65	42.65	46.75	59
l_s[mm]	5.6	5.7	9.8	8.2	7.35	8.2
Ring number	7	8	9	10	11	12
ρ_i[mm]	72.35	80.55	86.95	105	121	134
l_s[mm]	8.5	13.64	8.2	8.2	8.7	13.4

As w increases, the main lobe of the Bessel-Gauss beam does not change, but the sidelobes level increases. While k_ρ is increasing, the main lobe of the beam becomes narrow and the positions of the sidelobes are changed accordingly. It indicates that the attenuation factor $e^{-(\rho^2/w^2)}$ introduced by the Gaussian function mainly affects the sidelobes level, and the beamwidth of the main lobe and the position of the sidelobes are mainly affected by Bessel function $J_0(k_\rho\rho)$.

Due to the edge truncation, the antenna diameter of about 12 λ (28.8 cm@12.5 GHz) is selected [19]. Also, high order mode would be introduced by the large aperture, resulting in high sidelobes. In this design, the diameter of the antenna is chosen as 30 cm for low sidelobes and compact size. Besides, the beam waist w_0 =25mm and k_ρ = 0.6k_0 are chosen for low sidelobes, and the position of the Bessel-Gauss beam waist z is 50 mm. In this case, the null-null beamwidth (NNBW, the distance between the zeros of the main beam) of Bessel-Gauss is 30 mm, which is identical to that of the Bessel beam. Also, the maximum non-diffractive distance achieves 70 mm. As we can find that the maximum non-diffraction distance of Bessel beam deteriorates by using Gaussian beam modulation. This is because that a certain non-diffracting distance for Gaussian beam can be generated in the vicinity of the beam waist, but the beam would diffract at other positions [20]. The theoretical profiles of Bessel beam and Bessel-Gauss beam at z=50 mm are shown in Fig. 2(a), where the sidelobe levels of Bessel-Gauss beam are significantly lower than that of the Bessel beam due to the introduction of the factor $e^{-\rho^2/w^2}$.

III. Antenna Design

The optimization process in this work is divided into two steps: 1) To derive the target aperture field distribution, 2) To optimize the layout of the RLSA. To generate Bessel-Gauss pattern, the projection method is used to map the Bessel-Gauss pattern at a distance z=h (h is the position of the beam waist) onto the aperture [18]. Compared to the alternating projection method [21], the projection method in this design performs a simpler calculation, and no iterative algorithm is required, since the analytical solution of the derived aperture field is obtained during the projection process. By using the projection method, the target aperture field distribution can be derived by mapping the target Bessel-Gauss pattern to the antenna aperture, and the

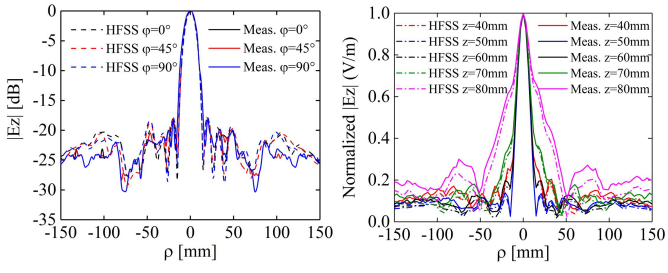

(a) (b)

Fig. 4. Simulated and measured normalized $|E|$ profiles. (a) At z = 50mm with different φ. (b) At different z with φ = 0°.

This article has been accepted for publication in a future issue of this journal, but has not been fully edited. Content may change prior to final publication. Citation information: DOI 10.1109/LAWP.2021.3115166, IEEE Antennas and Wireless Propagation Letters

derived aperture field distribution is the function of the aperture magnetic current distribution. On the parallel plate waveguide (PPW), each slot is equivalent to a magnetic dipole oriented along the slot length. The position of the slot fits the phase of the magnetic dipole moment, and the length of the slot fits the magnitude of the magnetic dipole moment. Through multiple iterations, the position and size of slots on each ring are adjusted to synthesize the magnetic dipole moment distribution of the target aperture field distribution [21].

For high solving effectiveness and to save memory space, the optimization is co-simulated using the commercial software MATLAB-HFSS. HFSS is used for the desired magnetic current distribution, and MATLAB is used to optimize the position and size of the slot cooperated with the results in HFSS. The detailed position (ρ_i) and length (l_s) of the slot are given by Table I.

A. RLSA Structure

The antenna consists of a parallel plate radial waveguide. F4B substrate with a permittivity ε_r=2.2 and a thickness h_p=3 mm is filled in the radial waveguide. The antenna is centrally fed by using a coaxial probe fixed on the back of the antenna to a 50 Ω SMA connector, as shown in Fig. 2(b). The inner conductor of the coaxial probe is connected to a metal disc with the radius of r_1 and thickness of h_1, which is attached in the center of the upper plate. By adjusting the size of the disc, good matching can be achieved. The final RLSA structure has a spillover efficiency and average aperture distribution error [21] of 95.1% and 2.7%, respectively.

B. Simulation and Measurement

The proposed RLSA antenna is fabricated, as shown in Fig. 2(b). The simulated/measured reflection coefficient $|S_{11}|$ is displayed in Fig. 3(a). It can be seen that good matching ($|S_{11}|$<-10 dB in the frequency of 12.44-12.56GHz/12.48-12.66GHz) can be achieved, which covers the operating frequency of 12.5 GHz. For the near-field normalized $|E_z|$ profiles, a VNA was used to measure the response of S-parameter. One port was connected to the antenna, and the other was connected to the probe. The probe was placed above the antenna to extract the z component of the electric field above the antenna over the area of 300×300 mm^2. Due to the center-feed structure, high-order Bessel function J_1 cannot be excited, and so E_ρ is 0, resulting in E=E_z. The normalized z component of the electric field is obtained by [22]:

$$|E_z|_{Normalized} = |E|_{Normalized} = \frac{|S_{21}|}{|S_{21}|_{\max}} \quad (2)$$

where $|S_{21}|$ is the magnitude of the transmission coefficient, and $|S_{21\max}|$ is the maximum magnitude value of the transmission coefficient among all the measures.

The simulated and measured normalized $|E_z|$ profile of the main beam along Oz-axis is displayed in Fig. 3(b). It can be seen that the simulated (measured) $|E_z|$ profile decreases along the propagation distance with non-diffractive range of 70 mm (70 mm), where the intensity of $|E_z|$ is declined by 3 dB. Within the maximum non-diffractive range of the Bessel-Gauss beam, the position of the beam waist z=50mm is included, which agrees with the theoretical design.

Also, the simulated and measured normalized $|E_z|$ profile at z=50 mm (within the non-diffractive distance) is displayed in Fig. 2 (a), where the desired Bessel-Gauss beam with low sidelobe levels is generated. However, the ripple of the simulated and measured Bessel-Gauss field is created, and the sidelobes are higher than the theoretical ones. The discrepancy can be mainly caused by the edged-diffracted waves arising from the aperture truncation [8].

Besides, the simulated (measured) $|E_z|$ profiles at the azimuthal planes φ=0°, 45° and 90° for z=50 mm is shown in Fig. 4(a), where NNBW of 30mm (30 mm) is achieved at the operation frequency of 12.5 GHz (12.5 GHz), and the peak sidelobe level -18.14dB (-18.07dB) is generated. Also, the profiles are nearly identical over different azimuthal planes, indicating that the generated beam is almost symmetrical. Furthermore, the simulated (measured) normalized $|E_z|$ profiles at the distances of z=40 mm, z=50 mm, z=60 mm, z=70 mm and z=80mm away from the antenna is displayed in Fig. 4(b). As

TABLE II
COMPARISON BETWEEN BESSEL-GAUSS ANTENNA AND OTHER SENSORS

Reference	Operating frequency	Defect depth	Detectable defect size
[3]	9.4GHz	-	1.857λ
[4]	10.5GHz	2mm@0.07λ	1.33λ
[5]	65GHz	Surface	0.87λ
Bessel-Gauss	12.5GHz	5mm@0.21λ	1.25λ

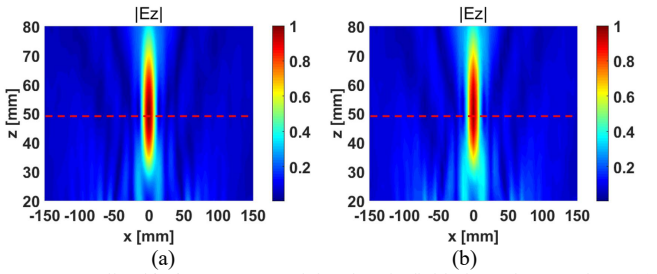

Fig. 5. Normalized $|E_z|$ component of the electric field along the *xoz*-plane. (a) 2-D simulated electric field. (b) 2-D measured electric field.

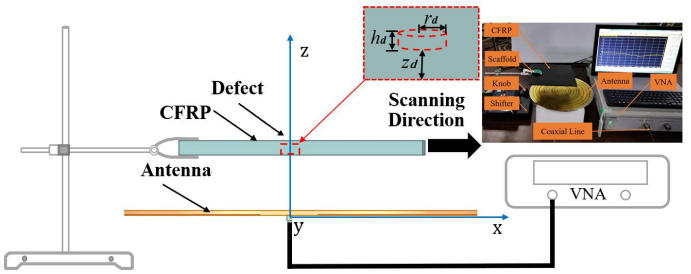

Fig. 6. Measurement setup. CFRP is fixed on the scaffold above the antenna and moves along the *x*-axis. The defect radius (r_d) is 15mm, and the defect height (h_d) is 5mm. The defect depth from the surface is z_d=5mm.

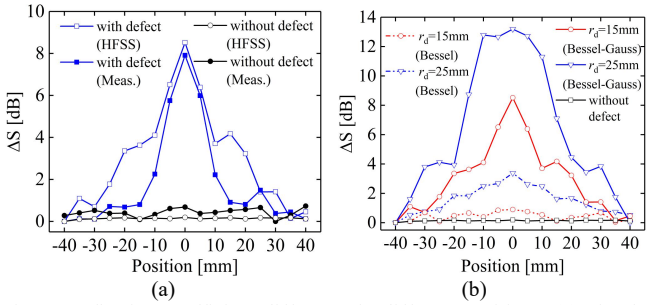

Fig. 7. Reflection coefficient difference in different positions. (a) Simulated and measured reflection coefficient difference with or without defects by using Bessel-Gauss antenna. (b) Simulated reflection coefficient difference for defect detection by using Bessel antenna and Bessel-Gauss antenna.

This article has been accepted for publication in a future issue of this journal, but has not been fully edited. Content may change prior to final publication. Citation information: DOI 10.1109/LAWP.2021.3115166, IEEE Antennas and Wireless Propagation Letters

distance increasing, the main beam property, i.e. Half Power Beamwidth (HPBW) and NNBW almost remains the same for the distances up to z=60 mm (60 mm), while the main beam starts to widen beyond the non-diffractive distance of z=70mm (70mm). Also, the simulated and measured 2-D plots of the normalized $|E_z|$ are shown in Fig. 5. It can be seen that the simulated and the measured Bessel-Gauss profiles are basically consistent. At the waist of the beam (z=50mm), the electric field intensity reaches the maximum and the peak sidelobe level is low.

IV. Non-metal Internal Defect Detection

The carbon fiber reinforced polymer (CFRP), which offers superior performance of high strength and high rigidity, is widely used to strengthen, renovate and repair aging bridges. However, in the long-term use process, the delamination and debonding are inevitable [23]. In this work, CFRP is chosen as the DUT, and it is uniformly distributed, except for the defects.

For near-field microwave NDT, the proposed antenna is fixed on a scaffold, and the CFRP is placed parallelly to the antenna at z=50 mm (within the maximum non-diffractive distance), where the sidelobe is low. Besides, the height of DUT is immersed in the main beam within the non-diffractive distance to avoid the misjudgment because of the change in main beam energy. To detect the defects, the reflection method is used [24]. The CFRP can be manually moved along x-axis with a step width of 5 mm, and one port of the VAN was connected to the antenna to record the reflection coefficient versus movements. The detection schematic diagram is displayed in Fig. 6, where a CFRP with a cylindrical inner defect (height and radius of defect are h_d and r_d) is taken as example.

The existence of defects would change the effective permittivity of the DUT, of which the imaginary part represents dielectric loss, resulting in a significant change in the reflection coefficient amplitude of antenna [6]. For the non-resonant sensor [5], the defect can be detected by monitoring the amplitude change, due to the insensitivity to the frequency shift. In this design, to evaluate the defect position, the absolute value of the reflection coefficients difference (ΔS) is defined, as expressed by

$$\Delta S=||S_{11}|_x-|S_{11}|_0| \quad (3)$$

where $|S_{11}|_x$ is the magnitude of reflection coefficient at the resonant frequency in different movement distances $x\epsilon$[-40:40]mm, and $|S_{11}|_0$ is that in the original position x=0.

Compared to simulated and measured ΔS at different movement distances, the defect position can be found, as shown in Fig. 7(a). Also, the simulated and measured ΔS of CFRP without inner defect is added in Fig. 7(a). It can be seen that the ΔS without defects is almost close to 0 dB at different distances. Having the defect, the ΔS changes significantly as the distance varies. At the center of the antenna, ΔS reaches to the maximum, indicating that the defects were detected in this area.

To verify the performance of Bessel-Gauss beam, the Bessel antenna with the same NNBW of 30 mm is used for near-field microwave NDT. The Bessel antenna works at the same resonant frequency of 12.5 GHz, but the first sidelobe level achieves only -8 dB, which is higher than that of the proposed Bessel-Gauss antenna. The ΔS at different movement distances is depicted in Fig. 7(b). It can be observed that when the defect radius is 15mm, ΔS of Bessel antenna fluctuates around 0 dB, resulting in failure of the defect position. When the defect radius increases to 25mm, the maximum ΔS of both Bessel antenna and Bessel-Gauss antenna is obtained at x=0, indicating that the defect position is detected successfully. Compared with the conventional Bessel antenna, the Bessel-Gauss antenna has a larger $\triangle S$ for detecting the same defect, and high sensitivity (small detectable size) can be achieved, which shows its superiority for detecting non-metal internal defects.

The comparisons of the detection effect between the Bessel-Gauss antenna and other sensors for non-metallic materials with defects are listed in Table II, where the Bessel-Gauss antenna achieves the largest detection depth. Although the detectable defect size by using Bessel-Gauss antenna is not the smallest, compare to the horn antenna in [5], which is used to detect the surface defects. Evidently, the proposed Bessel-Gauss antenna has the merits of large penetration depth and high sensitivity for internal defects of non-metal composite materials. Also, the comparison of the RLSA performance between the proposed Bessel-Gauss antenna and other Bessel antennas is listed in Table III, where the proposed Bessel-Gauss antenna achieves narrow beam width and low sidelobe levels. In addition, the proposed antenna has a narrow bandwidth, which is suitable for non-metallic defect detection that is sensitive to the frequency shift.

TABLE III
Comparison between Bessel-Gauss antennas and other RLSA antennas

Reference	Operating frequency	Radius (mm)	Band width	Sidelobe level(dB)	NNBW (mm)
[8]	30GHz	50@5λ	6.7%	-8	14@1.4λ
[9]	12.5GHz	150@6.25λ	6.7%	-13	40@1.67λ
[10]	15GHz	600@30λ	40%	-10	120@6λ
[11]	12.5GHz	250@10.4λ	24%	-10	40@1.67λ
[12]	10GHz	210@7λ	-	-10	39@1.3λ
This work	12.5GHz	150@6.25λ	1.4%	-18	30@1.25λ

V. Conclusion

A Bessel-Gauss RLSA antenna with characteristics of non-diffractive, narrow beam and low sidelobe levels has been proposed for near-field microwave NDT. The antenna is based on a parallel plate radial waveguide with slots on the metal upper surface. By using a projection method, the slot array layout is optimally arranged for the desired near field Bessel-Gauss pattern. Besides, the proposed antenna is used to detect internal defects of CFRP. The simulated and measured results showed that a large detection depth and high sensitivity can be achieved by the proposed Bessel-Gauss RLSA antenna for non-metal internal defects detection.

REFERENCES

[1] B. Harris, Fatigue in Composites: Science and Technology of the Fatigue Response of Fibre-Reinforced Plastics, Sawston, U.K.: Woodhead Publishing, Oct. 2003.

[2] A. Foudazi, C. A. Edwards, M. T. Ghasr and K. M. Donnell, "Active microwave thermography for defect detection of CFRP-strengthened cement-based materials," in *IEEE T Instrum Meas*, vol. 65, no. 11, pp. 2612-2620, Nov. 2016.

[3] S. Kharkovsky, A. C. Ryley, V. Stephen, and R. Zoughi, "Dual-polarized microwave near-field reflectometer for non-invasive inspection of carbon fiber reinforced polymer (CFRP) strengthened structures," *IEEE Instrum. Meas. Technol. Conf. Proc., 23rd*, pp. 24-27, Apr. 2006.

[4] D. Hughes, M. Kazemi, K. Marler, R. Zoughi, J. Myers, and A. Nanni, "Microwave detection of delaminations between fiber reinforced polymer (FRP) composite and hardened cement paste," *AIP Conference Proceedings*, May. 2002.

[5] S. H. Yang, K. B. Kim, H. G. Oh, and J. S. Kang, "Non-contact detection of impact damage in CFRP composites using millimeter-wave reflection and considering carbon fiber direction," *NDT & E International*, vol. 57, pp. 45-51, Apr. 2013.

[6] X. Yang, J. Chen, P. Su, X. Lei, J. Lei, Y. Xie, J. Yuan, and Z. Zhu, "Detection of defects in film-coated metals and non-metallic materials based on spoof surface plasmon polaritons," *IEEE Sens. J.*, vol. 19, no. 24, pp. 11891-11899, Dec. 2019.

[7] M. Balma, A. Mazzinghi, D. Devona, G. Guarnieri, G. Mauriello, M. Albani, and A. Freni, "Bessel beam generation with a RLSA antenna for non-contact detection of buried objects," *European Conference on Antennas & Propagation. IEEE*, pp. 762-766, Apr. 2014.

[8] S. C. Pavone, M. Ettorre, and M. Albani, "Analysis and design of bessel beam launchers: longitudinal polarization," *IEEE Trans. Antennas Propag.*, vol. 64, no. 6, pp. 2311-2318, Jun. 2016.

[9] M. Ettorre, S. C. Pavone, M. Casaletti and M. Albani, "Experimental validation of bessel beam generation using an inward hankel aperture distribution," *IEEE Trans. Antennas Propag.*, vol. 63, no. 6, pp. 2539-2544, June 2015.

[10] A. Mazzinghi et al., "Large depth of field pseudo-bessel beam generation with a rlsa antenna," *IEEE Trans. Antennas Propag.*, vol. 62, no. 8, pp. 3911-3919, Aug. 2014.

[11] D. Comite, G. Valerio, M. Albani, A. Galli, M. Casaletti, and M. Ettore, "Exciting vorticity through higher order Bessel beams with a radial-line slot-array antenna," IEEE Trans. Antennas Propag., vol. 65, no. 4, Apr. 2017.

[12] M. Albani, S. C. Pavone, M. Casaletti, and M. Ettorre, "Generation of non-diffractive Bessel beams by inward cylindrical traveling wave aperture distributions," *Optics Express*, 22(15):18354-64, Jul 2014.

[13] F. Gori, G. Guattari, and C. Padovani, "Bessel-gauss beams," *Optics communications*, pp. 491-495, Aug. 1987.

[14] P. L. Overfelt, and C. S. Kenney, "Comparison of the propagation characteristics of Bessel, Bessel–Gauss, and Gaussian beams diffracted by a circular aperture," *JOSA A*, pp. 732-745, May, 1991.

[15] D. De, and L. Xiao, "Approximate description for Bessel, Bessel–Gauss, and Gaussian beams with finite aperture," JOSA A, 16.6 (1999): 1286-1293.

[16] W. Fuscaldo, A. Benedetti, D. Comite, P. Burghignoli, and A. Galli, "Microwave synthesis of Bessel, Bessel–Gauss, and Gaussian beams: a fully vectorial electromagnetic approach," *International Journal of Wireless and Microwave Technologies*, pp. 1-7, Jan. 2021.

[17] W. Fuscaldo, A. Benedetti, D. Comite, P. Baccarelli, P. Burghignoli, and A. Galli, "Bessel-Gauss beams through leaky waves: focusing and diffractive properties," *Phys Rev Appl*, May. 2020.

[18] R. Piestun and J. Shamir, "Synthesis of three-dimensional light fields and applications," *Proc. IEEE,* vol. 90, no. 2, pp. 222–244, Feb. 2002.

[19] I. Iliopoulos, M. Casaletti, R. Sauleau, P. Pouliguen, P. Potier and M. Ettorre, "3-D shaping of a focused aperture in the near field," *IEEE Trans. Antennas Propag.*, vol. 64, no. 12, pp. 5262-5271, Dec. 2016.

[20] R. L. Nowack, "A tale of two beams: an elementary overview of Gaussian beams and Bessel beams," Stud. Geophys. Geod., vol. 56, no. 2, pp. 355-372, Jan. 2012.

[21] M. Ettorre, M. Casaletti, G. Valerio, R. Sauleau, L. L. Coq, S. C. Pavone, and M. Albani, "On the near-field shaping and focusing capability of a radial line slot array," *IEEE Trans. Antennas Propag.*, vol. 62, no. 4, pp. 1991-1999, Apr. 2014.

[22] P. Lu, D. Voyer, A. Breard, J. Huillery, B. Allard, X. L. Shi, and X. Yang, "Design of TE-polarized bessel antenna in microwave range using leaky-wave modes," *IEEE Trans. Antennas Propag.*, vol. 66, no. 1, pp. 32-41, Jan. 2018.

[23] X. E. Gros, and K. Takahashi, "Non-destructive characterization of delaminated areas at interfaces between plies in carbon fiber/epoxy laminates with Foucault currents," *Instrum. Sci. Technol.*, vol. 7, no. 3, pp. 177-192, Jan. 2000.

[24] H. Mei, J. Chen, X. Fu, L. Wang, and Z. Guan, "Microwave reflection method for composite insulator internal defect detection," *ACDC 2016. IET*, pp. 1-4, May. 2016.